

Microwave radiation at criticality in a hybrid Josephson array

Kristen W. Léonard,^{1,*} Anton V. Bubis,^{1,*} Melissa Mikalsen,² William F. Schiela,² Bassel H. Elfeky,² William M. Strickland,² Duc Phan,¹ Javad Shabani,² and Andrew P. Higginbotham^{3,1,†}

¹*Institute of Science and Technology Austria, Am Campus 1, Klosterneuburg, 3400, Austria*

²*Department of Physics, Center for Quantum Phenomena,
New York University, New York, NY, 10003, USA*

³*James Franck Institute and Department of Physics,
University of Chicago, 929 E 57th St, Chicago, Illinois 60637, USA*

Anomalous metallic behavior is often observed near superconductor-insulator quantum critical points and, if persistent to zero temperature, poses a challenge to current theories of metals [1]. One explanation for this behavior could be incomplete thermal equilibrium between the sample and the cryostat. However, despite decades of study, the temperature of an anomalous metal has not yet been measured. We introduce a new experimental probe by capturing microwave radiation emitted from the anomalous metal, using a two-dimensional array of superconductor-semiconductor hybrid Josephson junctions as a model system. The total emitted radiation exceeds the limits of thermodynamic equilibrium, and is well described by an elevated sample temperature. The extracted sample temperature matches the onset of anomalous metallic behavior. Additionally, we discover scaling behavior of radiative noise in the presence of an applied bias. Elements of our noise-scaling observations were predicted based on nonlinear critical field theories [2–4] and gauge-gravity duality between current noise and Hawking radiation from a black hole [5]. This work shows that, in a prominent model system, anomalous metallic behavior is a non-equilibrium effect, and opens a new frontier in the study of universal, non-equilibrium phenomena near quantum criticality.

A broad regime of low-temperature resistance saturation is commonly observed in proximity to the superconductor-insulator transition (SIT) [6–13]. This anomalous metallic regime occurs in a strikingly wide array of platforms and materials, including the Josephson-junction arrays under study in this work, behaves as a distinct thermodynamic phase [14], and challenges the theoretical understanding of metallic behavior at $T = 0$ K [1]. On the other hand, in several cases it has been experimentally shown that increased filtering restored a direct superconductor-insulator transition with no intervening metal, indicating that the anomalous metallic regime occurred due to a lack of thermalization [15, 16]. Currently, it is unclear whether anomalous metallic behavior reflects a lack of thermal equilibrium with the cryostat, crossover behavior, or a distinct thermodynamic phase of matter. We will show that this question can be resolved by measuring radiation emitted in the anomalous metallic regime.

Fundamentally, the non-equilibrium behavior of superconductor-insulator systems has been a subject of great theoretical interest. Owing to the presence of integrability in the limit of high energy density, arrays of Josephson junctions theoretically exhibit slow thermalization in the classical case [17, 18]. In the quantum case, many-body localized and multi-fractal metallic phases are predicted [19, 20]. Near the superconductor-insulator transition, analyses based on critical field theories [2–4] and gauge-gravity duality [5] have predicted that non-equilibrium noise is described by an effective tempera-

ture whose scaling with applied bias is controlled by the dynamical critical exponent. Testing these predictions requires an experimental probe of non-equilibrium behavior, moving beyond the traditional transport probes of superconductor-insulator physics.

Here, we answer this challenge by measuring microwave radiation proximal to the superconductor-insulator quantum phase transition, focusing on an array of superconductor-semiconductor hybrid Josephson junctions as a tunable model system [9, 11]. We observe excess radiation coincident with the onset of resistance saturation. Adapting methodology from the calibration of microwave radiometers [21], quantum-limited amplifiers [22], and axion haloscopes [23], we convert measured microwave noise power to an equivalent sample temperature. The extracted temperature is found to be compatible with the sample falling out of equilibrium with the cryostat in the anomalous metallic regime.

Motivated by predictions of universal scaling behavior near quantum critical points [2–5], we additionally probe non-equilibrium radiation in the presence of an applied bias. We discover that the noise-equivalent sample temperature exhibits scaling as a function of current, qualitatively reproducing theoretically anticipated behavior. Quantitatively however, our results deviate from the predictions in several ways, leaving open space for re-interpretation of theoretical estimates. With our apparatus we thereby demonstrate a new experimental path for studying the non-equilibrium response of quantum critical systems.

The key technical innovation of our experiment is to connect an anomalous metallic system to a microwave readout chain (Fig. 1a). Coupling capacitors allow microwave radiation (black arrow) to be efficiently col-

* Equal contribution

† ahigginbotham@uchicago.edu

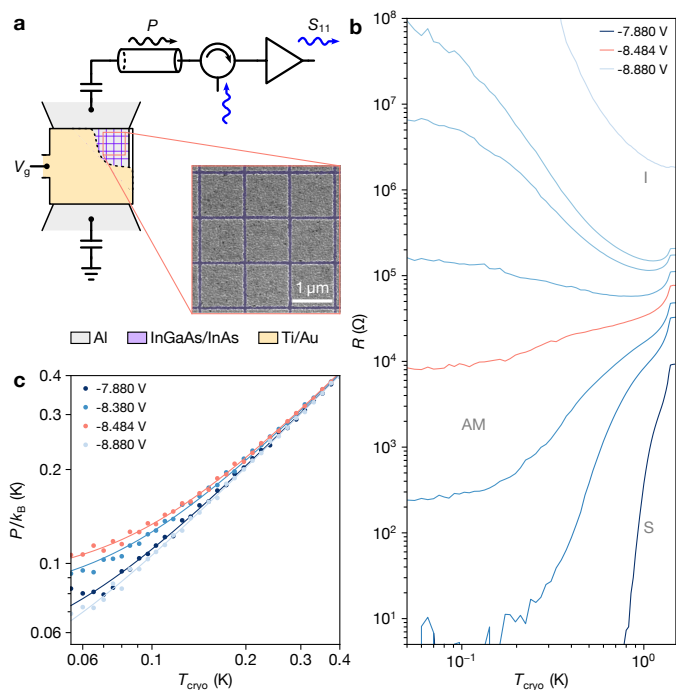


FIG. 1. **a**, Schematic of the device showing the Al/InAs Josephson junction array capacitively coupled to a microwave readout chain, with a top-gate to tune carrier density in the InAs two dimensional electron gas. A circulator and filtering (not pictured) prevents back-action noise from disrupting the anomalous metallic state, and allows it to be probed with a weak microwave tone. The incident microwave power spectral density P can also be measured. Standard quasi-four-probe transport measurement omitted from schematic for clarity. Scanning electron micrograph of the Al islands is shown in the inset. **b**, Measured resistance R versus cryostat temperature T_{cryo} at different top-gate voltages (indicated by colors). **c**, Measured radiation P as a function of T_{cryo} for selected top-gate voltages. The most excess radiation is observed at a top-gate voltage of -8.484 V, shown in panels **b** and **c** in salmon color. Solid lines are a model for an effective saturation radiation, P_{sat} , determined via best fit to each curve. The values of P_{sat}/k_B for each top-gate voltage are -7.88 V: 49 mK; -8.38 V: 76 mK; -8.484 V: 89 mK; -8.88 V: 37 mK.

lected and measured, while a circulator and filtering prevent back-action effects on the fragile anomalous metallic state. A two-dimensional array of superconductor/semiconductor Al/InAs Josephson junctions [24, 25] is formed from the two-dimensional electron gas situated in the 4 nm-thick InAs quantum well spaced 10 nm below the Al layer. Measurements of two devices (S1, S2) are presented, with all reported measurements from device S1 unless otherwise indicated. Device S1 consists of a 40 wide x 100 long array of Al squares with periodicity 1.15 μm , spaced by 0.08 μm (Fig. 1a), and device S2 has the same proportions as S1 but the opposite aspect ratio: a 100 wide x 40 long array of Al islands. In the superconducting regime these junctions are typically ballistic [25].

In both devices a 50 nm-thick Al top-gate is deposited over a 60 nm Al₂O₃ dielectric layer covering the entire array. The measurements were carried out in a dilution refrigerator with a base temperature of 50 mK. Noise measurements were carried out in a 10 MHz band around 1.42 GHz, and uncalibrated microwave reflection (S_{11} , blue arrows in Fig. 1a) was measured and averaged in the same frequency band. Microwave spectroscopy measurements were carried out in a wider band of 1.15–1.75 GHz defined by the cryogenic circulator. Standard quasi-four-probe resistance measurements were performed with an AC bias of 5 μV over the lines in the cryostat and the sample.

It is useful to categorize sample behavior based on the dependence of measured resistance on cryostat temperature. For modest top-gate voltages, resistance decreases sharply with temperature, falling below the measurement threshold of our equipment, indicating a superconducting state (S, Fig. 1b). In contrast, for more negative top-gate voltages resistance increases sharply with temperature, indicating insulating behavior (I, Fig. 1b). At intermediate top-gate voltages, there is an initial drop in resistance as the cryostat temperature is lowered, followed by a low-temperature saturation to a small but nonzero value (AM, Fig. 1b). This low-temperature saturation near the critical point of the SIT is the hallmark behavior of the anomalous metal. The observed superconducting, anomalous metallic, and insulating regimes qualitatively reproduce previous work on the same platform [11]. We have observed varying degrees of low-temperature saturation depending on sample and setup configurations (see Supplement). We have also verified that resistance saturation occurs in samples that are not connected to microwave circuitry.

The simultaneously measured microwave power spectral density P on the input of the measurement chain depends linearly on cryostat temperature for high T_{cryo} , as expected based on the thermal equilibrium relation $P = k_B T_{\text{cryo}}$ (Fig. 1c). At lower temperatures P saturates, indicating non-equilibrium behavior. The data are well described by a phenomenological equation with a gate voltage dependent saturation power P_{sat} , according to $P^2 = k_B^2 T_{\text{cryo}}^2 + P_{\text{sat}}^2$. The saturation power is largest when the sample is tuned near the critical resistance of the superconductor-insulator transition. Studying the excess, non-equilibrium noise near the SIT is the central focus of this work. In what follows, we demonstrate the origin of the excess noise and show how to interpret it in terms of an effective sample temperature.

A more detailed understanding of excess noise at the superconductor-insulator transition can be obtained by studying the system's evolution with gate voltage at fixed cryostat temperature. Measured device resistance increases with decreasing gate voltage (Fig. 2a). At lower temperatures, the increase in resistance becomes more dramatic, with isothermal resistance curves crossing at a resistance separatrix of approximately 60 k Ω , corresponding to a critical sheet resistance of 24 k Ω . For

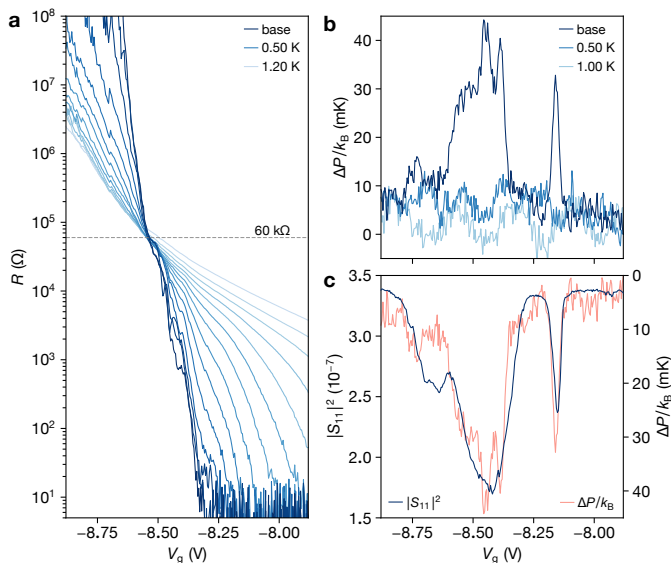


FIG. 2. **a**, Measured resistance R as a function of top-gate voltage V_g for different cryostat temperatures (indicated by colors). Resistance curves cross at the critical point indicated by the separatrix with resistance ≈ 60 k Ω (indicated). **b**, Excess noise ΔP versus V_g for different cryostat temperatures. ΔP is defined as the measured microwave power spectral density P minus the value measured deep in the superconducting phase, at the highest gate voltage in each trace; it represents the noise in excess of thermal-equilibrium expectations. Large excess noise is observed at low temperature (darkest blue trace). **c**, Reflection coefficient $|S_{11}|^2$ (left axis) and ΔP at 10 mK from panel **b** (right axis) versus V_g . Excess noise is strongly negatively correlated with $|S_{11}|^2$.

comparison, the (2+1)D XY model has a critical sheet resistance of 22.6 k Ω in the clean limit [26], and a smaller value of 12.9 k Ω in the disordered case [27]. Experimentally, critical points in other anomalous metallic systems have been reported at or near $h/4e^2 = 6.5$ k Ω [11, 28].

For elevated cryostat temperature, negligible excess noise is observed at all gate voltages, a signature expected for a system in equilibrium (Fig. 2b). However, at base temperature significant excess noise is observed, peaked slightly on the superconducting side of the SIT. Elevated radiation levels are observed throughout the anomalous metallic regime identified in Fig. 1b. These observations are compatible with the temperature-dependent noise study in Fig. 1b, and together indicate at the very least a broad region of non-equilibrium behavior surrounding the superconductor-insulator transition. Additionally, a solitary, sharp spike in excess noise is observed at -8.16 V, well within the ostensibly superconducting region.

Interestingly, excess noise is negatively correlated with the microwave reflection coefficient $|S_{11}|^2$ (Fig. 2c). Qualitatively, this correlation reflects the fact that noise generated by the sample can only be efficiently measured when the sample is impedance matched, $S_{11} = 0$. Note,

however, that S_{11} is weakly temperature dependent below 0.5 K, so that the temperature dependence in Fig. 2b should be attributed to a change in radiation, rather than a change in matching. More quantitatively, this observation leads us to propose a simple interpretation of the excess noise as arising from a device with an effective temperature T_s which is generally not equal to the cryostat temperature T_{cryo} . This model predicts a linear relationship between P and $|S_{11}|^2$

$$P/k_B = -\alpha|S_{11}|^2 (T_s - T_{\text{cryo}}) + T_s, \quad (1)$$

where α accounts for the net loss of the input lines and measurement chain, $\alpha|S_{11}|^2$ is the sample-referred reflection coefficient, and $\alpha|S_{11}|^2 = 1$ corresponds to complete reflection. A similar model was used in [29]. Although S_{11} and α are generally frequency dependent, we measure in a narrow band such that S_{11} is constant, with negligible frequency dependence in α expected.

To explore the noise model described above, we intentionally increase T_s by driving the sample out of equilibrium with a microwave tone far from our measurement band, measuring P and S_{11} for different drive strengths. In the absence of any drive, P and S_{11} are linearly related, consistent with the previously discussed correlations between noise power and microwave reflection (Fig. 3a). Under the application of a microwave drive at selected frequencies, P and $|S_{11}|^2$ maintain a linear relationship. Both the slope and vertical intercept increase with microwave drive power, while the intersection between curves is approximately drive-power independent. These observations have a straightforward interpretation within the noise model of Eq. 1. Both increasing vertical intercept and slope reflect an elevated sample temperature T_s , and a fixed crossing point at $-|S_{11}|^2 = 1/\alpha$ and $P/k_B = T_{\text{cryo}}$ reflects a constant T_{cryo} .

More formally, the best-fit slopes and vertical intercepts from Fig. 3a can be analyzed to extract α and the cryostat temperature T_{cryo} , as shown in Fig. 3b. The fit value of $\alpha = 64.5$ dB is compatible with an independent open-circuit calibration, and the fit value of $T_{\text{cryo}} = 50$ mK is self-consistent with the base cryostat temperature used in Fig. 2-4 to calculate P and T_s . We use this self-consistency criteria to define T_{cryo} . As a point of comparison, fixing α to the open-circuit calibration value of 63.9 dB yields a best-fit T_{cryo} of 28 mK. The linear relationship between P and $|S_{11}|^2$ and the compatibility of α and T_{cryo} with independent measurements gives evidence that Eq. 1 constitutes a predictive noise model for the device under study.

Using Eq. 1 and our calculated α and T_{cryo} , it is possible to make an inference of sample temperature from a microwave power spectral density (P) measurement. In the case of the anomalous metallic curve from Fig. 1b at -8.38 V, we find $T_s = 148$ mK, well above the base cryostat temperature determined either from the fits in Fig. 3a, by open circuit calibration, or by readings of the RuO $_x$ thermometer installed on the mixing chamber plate. This temperature coincides with the onset of

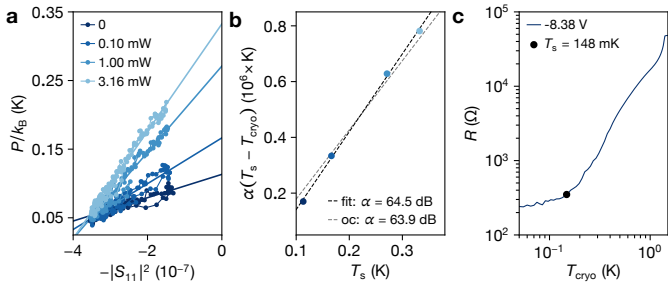


FIG. 3. **a**, Parametric plot of microwave power spectral density P vs microwave reflection $|S_{11}|^2$, both measured as a function of gate voltage. Power of microwave drive tone (at 547 MHz) at room temperature is indicated in legend; there is nominally 91 dB of attenuation between room temperature and the sample. A linear fit is performed to each curve to extract T_s and $\alpha(T_s - T_{\text{cryo}})$ according to Eq. 1. **b**, Slopes vs intercepts extracted from the fits to **a**. A subsequent linear fit (black) yields the net loss $\alpha = 64.5$ dB, and the cryostat temperature $T_{\text{cryo}} = 50$ mK. The fit from the independent open circuit calibration ('oc', gray) of 63.9 dB is also shown. Uncertainty is less than the marker size. **c**, Measured resistance as a function of cryostat temperature is shown for the trace at -8.38 V from Fig. 1b, displaying anomalous metallic resistance saturation. T_s as calculated from Eq. 1 using α , T_{cryo} from the fits is plotted on the resistance curve. Resistance saturation begins approximately at this temperature.

anomalous metallic behavior, as shown in Fig. 3d. Thus, the anomalous metallic behavior can be understood as a consequence of the sample falling out of equilibrium with the cryostat below ≈ 150 mK. To verify that this phenomenon is generic, we have checked that metallic resistance saturation occurring at the calculated T_s as a function of cryostat temperature is observed when a microwave or low frequency heating tone is applied (see Supplement). In a different measurement configuration, we have also studied a sample which showed a higher-temperature onset of anomalous metallic behavior, and found that it emits more radiative noise (see Supplement), again consistent with a non-equilibrium origin of resistance saturation.

Summarizing up to this point, a simple model of non-equilibrium sample temperature explains the excess noise observed at the SIT, the correlated structure between P and $|S_{11}|^2$, and the origin of anomalous metallic behavior in our device. The nature of the non-equilibrium steady-state, however, has not yet been thoroughly explored. In ordinary metals, non-equilibrium steady states driven by an applied bias carry signatures of carrier charges and their interactions [30]. Near the superconductor-insulator transition, it has been put forward that current fluctuations about the non-equilibrium steady states are universally determined by the dynamical critical exponent [2–5].

To explore this intriguing concept, we have studied the behavior of our device as a function of applied bias near the superconductor-insulator transition critical

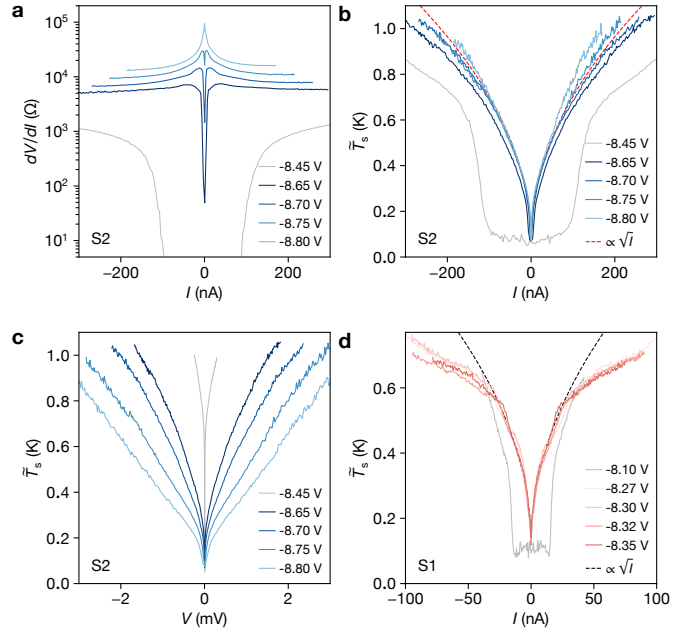


FIG. 4. **a**, Differential resistance dV/dI as a function of DC current, I , for different gate voltages (indicated by colors). Signatures of superconducting through insulating behavior are shown. **b**, Inferred sample temperature \tilde{T}_s as a function of measured DC current. Curves near criticality collapse onto one another. \sqrt{I} scaling shown, motivated by predictions [2–5]. **c**, Inferred \tilde{T}_s as a function of measured DC voltage, V . Curves do not collapse onto each other. **d**, Inferred \tilde{T}_s as a function of measured current in a second sample. Curves near criticality collapse onto one another. \sqrt{I} scaling shown, motivated by predictions [4, 5]. Panels **a** - **c** show data from device S2. Panel **d** shows data from device S1.

point. On the superconducting side of the SIT, resistance versus current I exhibits a pronounced zero-bias dip, whereas deep on the insulating side it exhibits a pronounced zero-bias peak (Fig. 4a). Over the same gate voltage and bias range, the non-equilibrium sample temperature \tilde{T}_s rises sharply with I . Here we have introduced \tilde{T}_s as an alternative inference of sample temperature in order to cancel out weak, time-dependent added noise drifts of the measurement chain (see Supplement). Expressing the total noise \tilde{T}_s in the units of current spectral density S_I , we estimate Fano factors F defined by $S_I = 2eFI$ [31] in the range 5 – 10, suggesting that heat does not leak and dissipate underneath the superconducting contacts [32]. Similar values were observed in earlier measurements of SNS junctions [29, 33, 34], which could microscopically arise from a combination of multiple Andreev reflections, Josephson radiation, or from the overheating of normal, diffusive regions between superconducting islands [35]. In contrast to resistance, whose zero-bias value varies by three orders of magnitude over the measured range of gate voltages, \tilde{T}_s is nearly gate voltage independent, and approximately collapses onto a

single nonlinear curve (Fig. 4b). The collapse only occurs when plotting \tilde{T}_s versus I ; other noise metrics such as the output noise power spectral density P or dependent variables such as voltage V , or Joule power IV do not exhibit a collapse (Fig. 4c). A qualitatively similar collapse is observed in a sample with a different geometry (Fig. 4d), confirming that it is a reproducible phenomenon.

The observed scaling behavior of \tilde{T}_s is reminiscent of theoretical predictions of universal non-equilibrium behavior near the SIT [2–5]. These theories predict that current fluctuations are described by an effective temperature, mimicking the fluctuation-dissipation relation even though the system is profoundly non-equilibrium. Furthermore, the effective temperature is predicted to exhibit a universal scaling with applied bias, similar to the experimental data reported in Fig. 4. Two additional experimental observations support a connection between non-equilibrium steady states and equivalent temperature. First, scaling in \tilde{T}_s in Fig. 4b,d occurs over a comparable temperature range to temperature-independence of near-critical curves in Fig. 1b. Second, zero-bias and high-bias differential resistance are comparable near the superconductor-insulator transition, where differential resistance is temperature independent (see Supplement). However, theories predict that the effective temperature scales as a function of applied voltage, in contrast to the experimentally observed scaling with current. It is unclear if this discrepancy is crucial, as these theories also predict a universal high-bias conductance linking current and voltage, while we observe a strong gate-dependent resistance [2, 3]. A full understanding of non-equilibrium responses near the SIT will require both further experimental work, for example varying sample sizes and model systems, as well as further theoretical input. However, these initial results indicate the appealing possibility of universal, non-equilibrium behavior near quantum criticality.

Several points need further clarification. Of relevance to Fig. 2b, we emphasize that the observed gate-voltage dependence of P is primarily explained by impedance matching effects; for extremal gate voltages where the device is mismatched, we cannot make an experimental statement about the sample temperature. Of relevance to Fig. 4, we give some additional discussion of the heat-sink mechanism in our samples. One possibility, sup-

ported by recent studies of single junctions [36], is that the primary thermalization mechanism is radiative. The observed scaling with bias current I might then suggest a picture of internal thermalization with Josephson radiation, which eventually escapes through the leads. When the device is driven normal by a magnetic field, our data are compatible with the more conventional thermalization electron-phonon bottleneck (see Supplement). Also of relevance to Fig. 4, we note that in contrast to the low-frequency resistance, the high-frequency conductivity is only weakly gate dependent. Weak gate dependence makes it experimentally convenient to extract the equivalent temperature from high-frequency noise data.

We have introduced microwave radiometry as a powerful probe of behavior near the superconductor-insulator transition. We find that the origin of anomalous metallic behavior in our system is due to a failure to thermalize with the cryostat. This finding raises non-equilibrium behavior at the superconductor-insulator transition as an important topic for systematic study. As a first step in this direction, we have measured equivalent non-equilibrium temperatures as a function of applied bias, discovering scaling behavior that was anticipated based on Keldysh, Boltzmann, and gravity-gauge duality approaches [2–5]. It would be interesting to perform further thermometry measurements in a wider variety of model systems. A possible scenario is that anomalous metallic behavior is due to poor thermalization only in some cases, with genuine metallic behavior as $T \rightarrow 0$ occurring in others [1, 37–39]. The experimental approach demonstrated here, combined with recently-demonstrated on-chip bolometry [36], sets the stage for a new exploration of non-equilibrium behavior in Josephson arrays, weak superconductors, and other near-critical systems.

We gratefully acknowledge feedback on the pre-print from Charles Marcus, Vadim Khrapai, Joel Moore, Andrew Green, Shivaji Sondhi, and Rufus Boyack. This work was primarily supported by the NOMIS foundation. This work was partially supported by the University of Chicago Materials Research Science and Engineering Center, which is funded by the National Science Foundation under award number DMR-2011854, and by the SFB Q-M&S funded by the Austrian Science Fund (FWF). We acknowledge technical support from the Nanofabrication Facility and the MIBA machine shop at IST Austria.

-
- [1] A. Kapitulnik, S. A. Kivelson, and B. Spivak, Colloquium: Anomalous metals: Failed superconductors, *Rev. Mod. Phys.* **91**, 011002 (2019).
 - [2] D. Dalidovich and P. Phillips, Nonlinear transport near a quantum phase transition in two dimensions, *Phys. Rev. Lett.* **93**, 027004 (2004).
 - [3] A. G. Green and S. L. Sondhi, Nonlinear quantum critical transport and the schwinger mechanism for a superfluid-mott-insulator transition of bosons, *Phys. Rev. Lett.* **95**, 267001 (2005).
 - [4] A. G. Green, J. E. Moore, S. L. Sondhi, and A. Vishwanath, Current noise in the vicinity of the 2d superconductor-insulator quantum critical point, *Phys. Rev. Lett.* **97**, 227003 (2006).
 - [5] J. Sonner and A. G. Green, Hawking radiation and nonequilibrium quantum critical current noise, *Phys. Rev. Lett.* **109**, 091601 (2012).
 - [6] H. M. Jaeger, D. B. Haviland, B. G. Orr, and A. M. Goldman, Onset of superconductivity in ultrathin granular metal films, *Phys. Rev. B* **40**, 182 (1989).

- [7] D. Ephron, A. Yazdani, A. Kapitulnik, and M. R. Beasley, Observation of quantum dissipation in the vortex state of a highly disordered superconducting thin film, *Phys. Rev. Lett.* **76**, 1529 (1996).
- [8] O. Crauste, C. A. Marrache-Kikuchi, L. Bergé, D. Stanescu, and L. Dumoulin, Thickness dependence of the superconductivity in thin disordered nbsi films, *Journal of Physics: Conference Series* **150**, 042019 (2009).
- [9] S. Eley, S. Gopalakrishnan, P. M. Goldbart, and N. Mason, Approaching zero-temperature metallic states in mesoscopic superconductor–normal–superconductor arrays, *Nature Physics* **8**, 59 (2012).
- [10] Z. Han, A. Allain, H. Arjmandi-Tash, K. Tikhonov, M. Feigel'man, B. Sacépé, and V. Bouchiat, Collapse of superconductivity in a hybrid tin–graphene josephson junction array, *Nature Physics* **10**, 380 (2014).
- [11] C. G. L. Böttcher, F. Nichele, M. Kjaergaard, H. J. Suominen, J. Shabani, C. J. Palmstrøm, and C. M. Marcus, Superconducting, insulating and anomalous metallic regimes in a gated two-dimensional semiconductor–superconductor array, *Nature Physics* **14**, 1138 (2018).
- [12] C. G. L. Böttcher, F. Nichele, J. Shabani, C. J. Palmstrøm, and C. M. Marcus, Dynamical vortex transitions in a gate-tunable two-dimensional josephson junction array, *Phys. Rev. B* **108**, 134517 (2023).
- [13] K. Ienaga, Y. Tamoto, M. Yoda, Y. Yoshimura, T. Ishigami, and S. Okuma, Broadened quantum critical ground state in a disordered superconducting thin film, *Nature Communications* **15**, 2388 (2024).
- [14] C. G. L. Böttcher, F. Nichele, J. Shabani, C. J. Palmstrøm, and C. M. Marcus, The berezinskii-kosterlitz-thouless transition and anomalous metallic phase in a hybrid josephson junction array, arXiv preprint (2022), arXiv:2210.00318 [cond-mat.mes-hall].
- [15] I. Tamir, A. Benyamini, E. J. Telford, F. Gorniaczyk, A. Doron, T. Levinson, D. Wang, F. Gay, B. Sacépé, J. Hone, K. Watanabe, T. Taniguchi, C. R. Dean, A. N. Pasupathy, and D. Shahar, Sensitivity of the superconducting state in thin films, *Science Advances* **5**, eaau3826 (2019), <https://www.science.org/doi/pdf/10.1126/sciadv.aau3826>.
- [16] J. Shin, S. Park, and E. Kim, Effect of external electromagnetic radiation on the anomalous metallic behavior in superconducting thin films, *Phys. Rev. B* **102**, 184501 (2020).
- [17] T. Mithun, Y. Kati, C. Danieli, and S. Flach, Weakly nonergodic dynamics in the gross-pitaevskii lattice, *Phys. Rev. Lett.* **120**, 184101 (2018).
- [18] T. Mithun, C. Danieli, Y. Kati, and S. Flach, Dynamical glass and ergodization times in classical josephson junction chains, *Phys. Rev. Lett.* **122**, 054102 (2019).
- [19] M. Pino, L. B. Ioffe, and B. L. Altshuler, Nonergodic metallic and insulating phases of josephson junction chains, *Proceedings of the National Academy of Sciences* **113**, 536 (2016), <https://www.pnas.org/doi/pdf/10.1073/pnas.1520033113>.
- [20] M. Pino, V. E. Kravtsov, B. L. Altshuler, and L. B. Ioffe, Multifractal metal in a disordered josephson junctions array, *Phys. Rev. B* **96**, 214205 (2017).
- [21] R. H. Dicke, R. Beringer, R. L. Kyhl, and A. B. Vane, Atmospheric absorption measurements with a microwave radiometer, *Phys. Rev.* **70**, 340 (1946).
- [22] M. A. Castellanos-Beltran, K. D. Irwin, G. C. Hilton, L. R. Vale, and K. W. Lehnert, Amplification and squeezing of quantum noise with a tunable josephson metamaterial, *Nature Physics* **4**, 929 (2008).
- [23] B. M. Brubaker, L. Zhong, Y. V. Gurevich, S. B. Cahn, S. K. Lamoreaux, M. Simanovskaia, J. R. Root, S. M. Lewis, S. Al Kenany, K. M. Backes, I. Urdinaran, N. M. Rapidis, T. M. Shokair, K. A. van Bibber, D. A. Palken, M. Malnou, W. F. Kindel, M. A. Anil, K. W. Lehnert, and G. Carosi, First results from a microwave cavity axion search at 24 μeV , *Phys. Rev. Lett.* **118**, 061302 (2017).
- [24] J. Shabani, M. Kjaergaard, H. J. Suominen, Y. Kim, F. Nichele, K. Pakrouski, T. Stankevic, R. M. Lutchyn, P. Krogstrup, R. Feidenhans'l, S. Kraemer, C. Nayak, M. Troyer, C. M. Marcus, and C. J. Palmstrøm, Two-dimensional epitaxial superconductor–semiconductor heterostructures: A platform for topological superconducting networks, *Phys. Rev. B* **93**, 155402 (2016).
- [25] W. Mayer, J. Yuan, K. S. Wickramasinghe, T. Nguyen, M. C. Dartiailh, and J. Shabani, Superconducting proximity effect in epitaxial Al-InAs heterostructures, *Applied Physics Letters* **114**, 103104 (2019), https://pubs.aip.org/aip/apl/article-pdf/doi/10.1063/1.5067363/19772789/103104_1_online.pdf.
- [26] M.-C. Cha, M. P. A. Fisher, S. M. Girvin, M. Wallin, and A. P. Young, Universal conductivity of two-dimensional films at the superconductor-insulator transition, *Phys. Rev. B* **44**, 6883 (1991).
- [27] M. Swanson, Y. L. Loh, M. Randeria, and N. Trivedi, Dynamical conductivity across the disorder-tuned superconductor-insulator transition, *Phys. Rev. X* **4**, 021007 (2014).
- [28] D. B. Haviland, Y. Liu, and A. M. Goldman, Onset of superconductivity in the two-dimensional limit, *Phys. Rev. Lett.* **62**, 2180 (1989).
- [29] P. Dieleman, H. G. Bukkems, T. M. Klapwijk, M. Schicke, and K. H. Gundlach, Observation of andreev reflection enhanced shot noise, *Phys. Rev. Lett.* **79**, 3486 (1997).
- [30] A. H. Steinbach, J. M. Martinis, and M. H. Devoret, Observation of hot-electron shot noise in a metallic resistor, *Phys. Rev. Lett.* **76**, 3806 (1996).
- [31] Y. Blanter and M. Büttiker, Shot noise in mesoscopic conductors, *Physics Reports* **336**, 1 (2000).
- [32] A. Denisov, A. Bubis, S. Piatrusha, N. Titova, A. Nasibulin, J. Becker, J. Treu, D. Ruhstorfer, G. Koblmüller, E. Tikhonov, and V. Khrapai, Heat-mode excitation in a proximity superconductor, *Nanomaterials* **12**, 10.3390/nano12091461 (2022).
- [33] Y. Ronen, Y. Cohen, J.-H. Kang, A. Haim, M.-T. Rieder, M. Heiblum, D. Mahalu, and H. Shtrikman, Charge of a quasiparticle in a superconductor, *Proceedings of the National Academy of Sciences* **113**, 1743 (2016), <https://www.pnas.org/doi/pdf/10.1073/pnas.1515173113>.
- [34] T. Hoss, C. Strunk, T. Nussbaumer, R. Huber, U. Staufer, and C. Schönenberger, Multiple andreev reflection and giant excess noise in diffusive superconductor/normal-metal/superconductor junctions, *Phys. Rev. B* **62**, 4079 (2000).
- [35] H. Courtois, M. Meschke, J. T. Peltonen, and J. P. Pekola, Origin of hysteresis in a proximity josephson junction, *Phys. Rev. Lett.* **101**, 067002 (2008).
- [36] B. Karimi, G. O. Steffensen, A. P. Higginbotham, C. M. Marcus, A. Levy Yeyati, and J. P. Pekola, Bolometric

- detection of josephson radiation, *Nature Nanotechnology* **10**, 1038/s41565-024-01770-7 (2024).
- [37] M. Feigel'man and A. Larkin, Quantum superconductor-metal transition in a 2d proximity-coupled array, *Chemical Physics* **235**, 107 (1998).
- [38] B. Spivak, A. Zyuzin, and M. Hruska, Quantum superconductor-metal transition, *Phys. Rev. B* **64**, 132502 (2001).
- [39] B. Spivak, P. Oretto, and S. A. Kivelson, Theory of quantum metal to superconductor transitions in highly conducting systems, *Phys. Rev. B* **77**, 214523 (2008).
- [40] F. Giazotto, T. T. Heikkilä, A. Luukanen, A. M. Savin, and J. P. Pekola, Opportunities for mesoscopics in thermometry and refrigeration: Physics and applications, *Rev. Mod. Phys.* **78**, 217 (2006).
- [41] A. J. Rimberg, T. R. Ho, i. m. c. Kurdak, J. Clarke, K. L. Campman, and A. C. Gossard, Dissipation-driven superconductor-insulator transition in a two-dimensional josephson-junction array, *Phys. Rev. Lett.* **78**, 2632 (1997).
- [42] A. Goldman, Superconductor-insulator transitions in the two-dimensional limit, *Physica E: Low-dimensional Systems and Nanostructures* **18**, 1 (2003), 23rd International Conference on Low Temperature Physics (LT23).
- [43] N. P. Breznay, M. A. Steiner, S. A. Kivelson, and A. Kapitulnik, Self-duality and a hall-insulator phase near the superconductor-to-insulator transition in indium-oxide films, *Proceedings of the National Academy of Sciences* **113**, 280 (2016), <https://www.pnas.org/doi/pdf/10.1073/pnas.1522435113>.
- [44] N. P. Breznay and A. Kapitulnik, Particle-hole symmetry reveals failed superconductivity in the metallic phase of two-dimensional superconducting films, *Science Advances* **3**, e1700612 (2017).

SUPPLEMENTAL

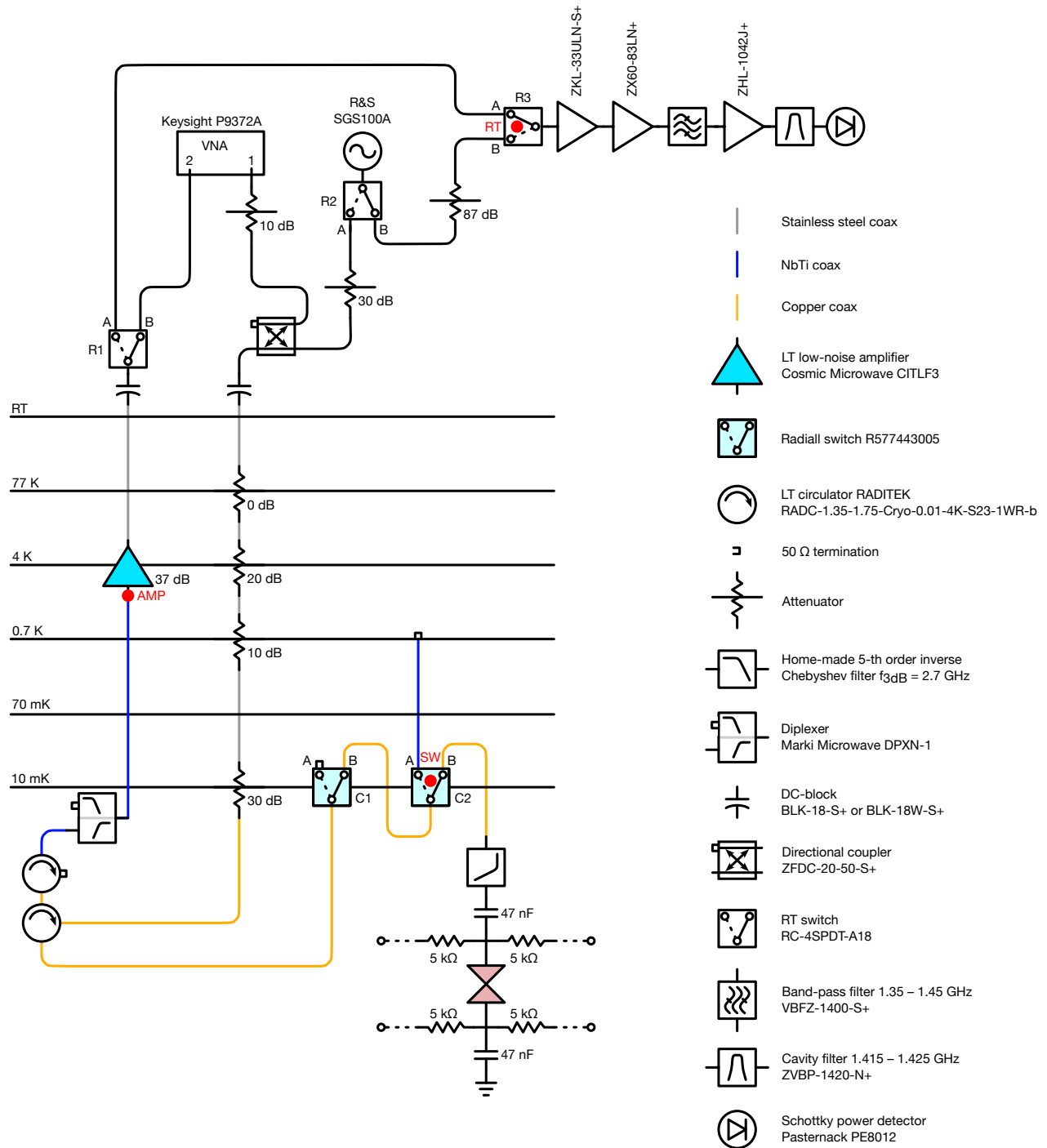


FIG. S1. **Experimental setup used in this work.** All elements located below the horizontal line designated with ‘RT’ are installed within the dilution refrigerator. Microwave signals from the VNA are attenuated by 10 dB and then coupled to the sample via RF directional coupler with 20 dB of insertion loss. Microwave signals from a signal generator are sent through 30 dB of attenuation before entering the fridge. A highly attenuated line leading to a circulator on the 10 mK stage of the fridge brings microwave signals to the sample. The sample is shown on the lower right-hand side by a circuit schematic. Two switches (C1, C2) are installed on the 10 mK stage which allow radiation from either the sample, a 50 Ω cap on the 700 mK stage, or from a 50 Ω cap on the 10 mK stage to be transmitted to the low-temperature amplifier on the 4 K stage. The low-temperature amplifier has a noise temperature of approximately 4 K and gain of about 35 dB at 1 GHz. Radiation is amplified at 4 K stage and then transmitted to the room temperature amplification chain. Radiation is measured with a power diode.

Calibration

Fig. S1 shows the setup of components installed at room temperature and inside the dilution refrigerator used in this work. We perform two types of calibration procedures. The first is to rule out the weak drift of the room temperature (RT) amplifiers. In Fig. S2a, noise power as measured by the power diode (in volts) is plotted as a function of time, while the nominal power on the input of the room temperature chain is constant. We observe two timescales of drift, the first being fast oscillations with a period of about 30 minutes. The second timescale is a slow drift of the envelope of the fast oscillations on a timescale of tens of hours. The amplitude of the fast oscillations is about 15 mK when converted to temperature units. We attribute these effects either to temperature variations in the laboratory room or to a slow drift of the various power supplies or other equipment.

To effectively remove these drifts, we measure a responsivity curve of the RT chain at each data point. We use the signal generator with a frequency of 1.42 GHz (center of the cavity filter band) to sweep over a range of output powers that cover the range of the noise powers (in volts) irradiated from the fridge (switch ‘RT’ is in position ‘B’ in Fig. S1). Then we flip the switch to position ‘A’ and measure noise power emitted from the fridge through the same chain as the signal generator power. This makes it possible to match an output voltage of the power diode to a corresponding power in watts at the point ‘RT’ in the diagram. Ideally, this removes the fluctuations due to a drift in the room temperature amplification chain, as shown in Fig. S2b. The blue curve is the same voltage shown in panel a, but it has been calibrated by a responsivity curve taken at time $t = 0$ s. The orange curve is the same data, but calibrated at each data point by a responsivity curve taken at the same time. The long term drift has been effectively eliminated, and the short term oscillations are greatly reduced. The amplitude of oscillations of the orange trace is about 4 mK in temperature units.

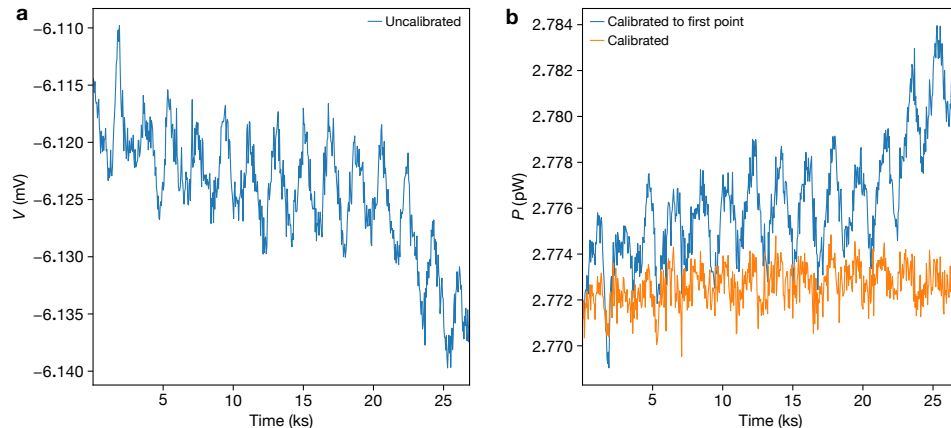


FIG. S2. **Responsivity curve calibration.** **a** The drift in measured noise on the power diode as a function of time. **b** The effect of performing a responsivity calibration to reduce drifts. The blue trace is the same data shown in panel a, but using a responsivity curve taken at the first point to calibrate the whole trace. The orange trace is the same data but with a responsivity curve taken at each time point and used to calibrate each point.

The second calibration procedure we apply is done to convert the noise power at ‘RT’ measured in watts into temperature units at point ‘SW’, see diagram in Fig. S1. To do this, we measure the radiation emanating from the sample (at 0 gate voltage), from the 50 Ω cap on the 700 mK ‘still’ stage, and from the 50 Ω cap on the mixing chamber stage as a function of temperature from base (~ 50 mK) to 1 K.

The results of these measurements are shown in Fig. S3. In the left panel, the measured noise power (referred to the point ‘RT’ as described above) is plotted as a function of the temperature of the stage where the sample or 50 Ω cap is located, i.e. the sample and 50 Ω cap on the mixing chamber stage are plotted versus the temperature of the mixing chamber stage (T_{cryo}) as it is swept from base temperature to 1 K and the noise from the 50 Ω cap on the still stage is plotted versus the temperature of the still stage as the temperature of the mixing chamber is swept from base to 1 K.

In the right panel, all measured noise is plotted as a function of T_{cryo} stage. Although it is intuitive that noise power emitted from the load should be proportional to the load temperature, we see in Fig. S3a that this is not the case for the load located on the still stage. This discrepancy can be eliminated if a loss, η , between the ‘SW’ and ‘AMP’ points is introduced. This loss couples irradiation from the load on the still plate with the irradiation from the bath with T_{cryo} , where we implied that the bath temperature is T_{cryo} because all the lossy components are installed

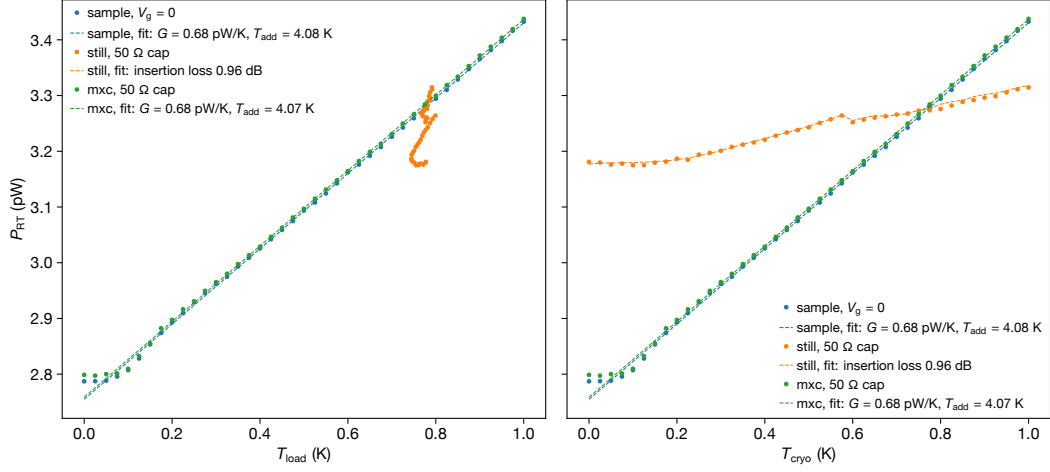


FIG. S3. **Details on chain calibration.** We calibrate the gain G and added noise temperature T_{add} of LTA, and insertion loss η . The left panel shows the noise measured from the sample, the 50Ω cap on the 700 mK (‘still’) stage, and the 50Ω cap on the mixing chamber stage as a function of the temperature of their stage, T_{load} . The right panel shows the same quantities but plotted as a function of the temperature of the mixing chamber stage, T_{cryo} . The gain found by linear fit to the sample and 50Ω cap on the mixing chamber stage data corresponds to $G = 36.9$ dB (for 10 MHz measurement band) and is in good agreement with manufacturer specs.

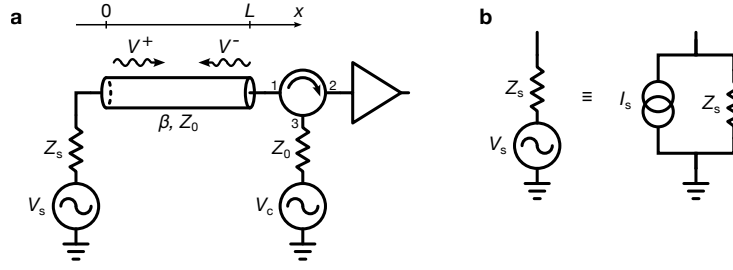


FIG. S4. **Circuit model schematic.** **a** Voltage generator model for our circuit. **b** Equivalent current generator circuit.

on the mixing chamber plate. Thus, the suggestive model to convert power in watts to temperature units is:

$$P_{\text{still}}/k_B = G(1 - \eta)T_{\text{still}} + G\eta T_{\text{cryo}} + GT_{\text{add}} \quad (2)$$

$$P_{\text{cryo}}/k_B = G(T_{\text{cryo}} + T_{\text{add}}) \quad (3)$$

where P_{still} is the noise power measured at the point ‘RT’ coming from the 50Ω cap on the still stage, G is the gain of the low temperature amplifier, η is the loss between the points ‘SW’ and ‘AMP’, T_{still} is the temperature of the still stage, T_{cryo} is the temperature of the mixing chamber stage, T_{add} is the added noise temperature of low temperature amplifier, and P_{cryo} is the noise measured at ‘RT’ coming from the 50Ω cap on the mixing chamber stage or from the sample (for a sample which is in equilibrium with the fridge).

The gain G and added noise temperature T_{add} of the low temperature amplifier are extracted from the slope and intercept of the linear fit to Eq. 3. The insertion loss η is extracted from the least-squares fit to Eq. 2, using the G and T_{add} found from fitting to Eq. 3. The values extracted from these fits are shown in the legend of Fig. S3. We repeat this calibration procedure for each cooldown and find similar but slightly different values for each fitting parameter, and use those values for calculating the excess noise in temperature units P/k_B , and the sample temperatures T_s reported in the main text. The values we obtain fall within manufacturer specifications.

Circuit theory

Figure S4a shows a schematic of a simplified model circuit for our measurement. A sample modeled as a voltage generator V_s with output impedance Z_s is connected to a transmission line of characteristic impedance Z_0 and propagation constant β . The transmission line has a left-moving scattering state $V^-(x) = V^- e^{i\beta x}$ and right-moving

scattering state $V^+(x) = V^+e^{-i\beta x}$. An ideal circulator followed by an impedance-matched amplifier is used to measure $V^+(L)$. The third port of the circulator is terminated by a matched load Z_0 , with an effective Johnson-Nyquist voltage generator V_c .

Applying Ohm's law to the third port of the circulator yields

$$V^-(L) = V_c/2, \quad (4)$$

as one might expect for a generator with a matched load. Current conservation for the sample connected to a transmission line reads:

$$\frac{V_s - (V^+(0) + V^-(0))}{Z_s} = \frac{V^+(0) - V^-(0)}{Z_0}, \quad (5)$$

where we have used the fact that the current through the transmission line $I(x) = (V^+(x) - V^-(x))/Z_0$ with the positive direction of the current being towards the right. Rearranging Eq. 5 gives

$$V^+(0) = V^-(0) \frac{Z_s - Z_0}{Z_s + Z_0} + V_s \frac{Z_0}{Z_s + Z_0}.$$

Finally, rewriting this equation at $x = L$ and substituting Eq. 4 we obtain

$$V^+(L) = \frac{V_c}{2} \frac{Z_s - Z_0}{Z_s + Z_0} e^{-2i\beta L} + V_s \frac{Z_0}{Z_s + Z_0} e^{-i\beta L}. \quad (6)$$

The first term on the right-hand side is the reflected wave generated by the load of the circulator, and the second is the wave generated by the sample's voltage generator. The voltage spectral density seen by the amplifier measured in the frequency band Δf is $S_V^+ = \langle V^+(L)^2 \rangle / \Delta f$, which can be expressed as

$$S_V^+ = \frac{S_V^c}{4} \left| \frac{Z_s - Z_0}{Z_s + Z_0} \right|^2 + S_V^s \left| \frac{Z_0}{Z_s + Z_0} \right|^2, \quad (7)$$

where we have used the fact that V_c and V_s are uncorrelated. The Johnson-Nyquist sample temperature is defined through $S_V^s = 4k_B T_s \text{Re}[Z_s]$ and the circulator temperature through $S_V^c = 4k_B T_c Z_0$. These quantities are related to the measured input power spectral density $P = S_V^+ / Z_0$ by

$$P = k_B T_c |S_{11}|^2 + k_B T_s (1 - |S_{11}|^2), \quad (8)$$

where the reflection coefficient for the sample S_{11} can be expressed as usual via the sample impedance Z_s as $S_{11} = \frac{Z_s - Z_0}{Z_s + Z_0}$. Incorporating the net loss α gives Eq. 1 in the main text. Note that the result depends only on the magnitude of reflection $|S_{11}|$, so a phase calibration is not needed.

Alternatively, the sample noise can also be expressed as arising from an equivalent current generator, as indicated in Fig. S4b. The current noise spectral density S_I is related to the sample voltage noise spectral density by $S_I^s = S_V^s / |Z_s|^2$. Substituting into Eq. 7 and using the same temperature definitions results in

$$P = k_B T_c |S_{11}|^2 + S_I^s Z_0 \frac{|Z_s|^2}{|Z_s + Z_0|^2}. \quad (9)$$

We see that for samples with real impedance Z_s when $Z_s \gg Z_0$ the measured power spectral density directly gives S_I^s , $P \approx k_B T_c + S_I^s Z_0$. However in the general case, both the magnitude and phase of S must be known

$$P = k_B T_c |S_{11}|^2 + \frac{1}{4} S_I^s Z_0 |1 + S_{11}|^2. \quad (10)$$

Fano factors are estimated from the measured data using the above equation. The phase of S_{11} is estimated based on a comparison with a distributed RC model in the normal state.

Reflection coefficient at high temperatures

In Fig. 2 in the main text we show the base temperature gate dependence of the reflection coefficient $|S_{11}|^2$. We show here that $|S_{11}|^2$ retains the same magnitude of gate dependence over a large temperature range. Fig. S5 shows essentially unchanged gate dependence of the main dip centered around -8.4 V in $|S_{11}|^2$ over the range of base to approximately 500 mK. At higher temperatures the structure of the gate dependence begins to change significantly. The dip around -8.1 V at base temperature begins to disappear before 500 mK. Only minor changes in the structure of $|S_{11}|^2$ are observed before the temperature at the onset of resistance saturation (approximately 150 mK).

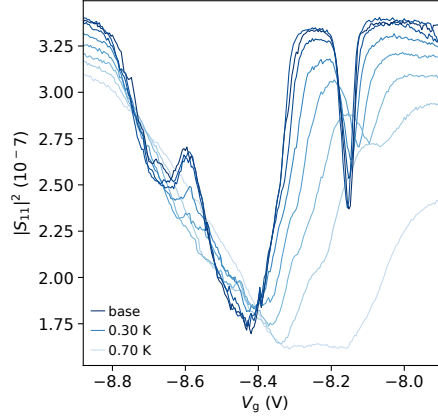


FIG. S5. **Reflection gate dependence at higher temperatures.** $|S_{11}|^2$ is plotted as a function of gate voltage for temperatures spanning from base (set point 0 mK) to 700 mK in 100 mK increments. The temperatures are indicated by colors as shown in the legend.

Added noise

In addition to the analysis performed in Fig. 3 in the main text, we also applied a driving tone during a temperature sweep. We measure resistance as a function of cryostat temperature, and observe the onset of resistance saturation occurring at higher cryostat temperatures for higher driving tones, as shown in Fig. S6a. The cryostat temperatures at the onset of resistance saturation, as well as the calculated sample temperatures at base cryostat temperature of approximately 300 – 400 mK are consistent with the analysis performed in the main text. The application of microwave radiation to the sample reproduces the saturating behavior of typical anomalous metal samples.

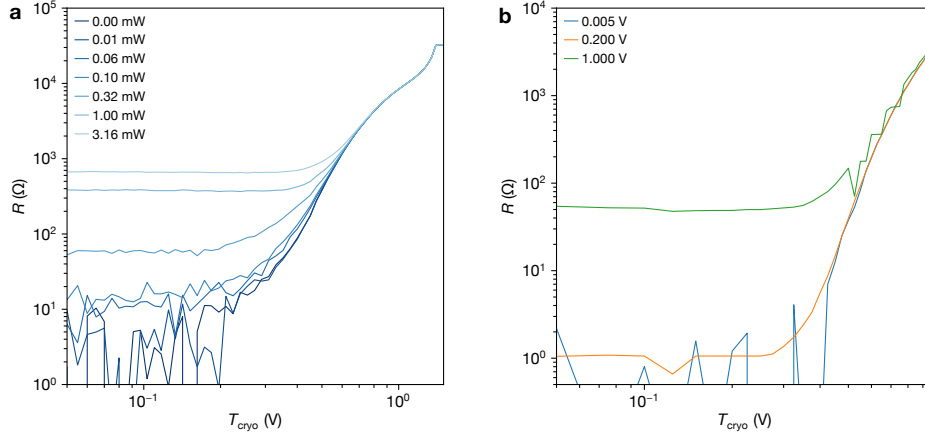


FIG. S6. **Resistance saturation under added noise.** **a** Sample resistance as a function of cryostat temperature for various drive tone powers at 200 MHz is shown. The resistance saturation associated with the anomalous metal increases with increasing drive tone power. The sample is driven from a base temperature superconducting state to an anomalous metallic state with a resistance saturation onset temperature of approximately 400 mK. **b** Resistance as a function of cryostat temperature is plotted for a 21.55 Hz tone applied with amplitudes of 0.005, 0.2, and 1 V. The sample is driven from the superconducting state to an anomalous metal state with onset of resistance saturation at about 300 – 350 mK.

We also apply a driving tone at lower frequencies. Shown in Fig. S6b, we increase the amplitude of a 21.55 Hz tone from 5 mV to 1 V, corresponding to an increase from 5 μ V to 1 mV across the lines of the cryostat and the sample. The low frequency drive also stimulates resistance saturation in this device. The sample is driven from a superconducting state to a resistive, anomalous metallic state, whose resistance saturation begins around 300 – 400 mK. This shows that a low frequency noise in an experimental setup could also produce behavior consistent with the anomalous metal.

Finite bias noise

In Fig. 4 in the main text we showed that the measured noise collapses to scaling behavior when plotted versus current, and not when plotted versus voltage. Here, in Fig. S7, we show that this behavior is reproduced in both samples. The dramatic collapse observed when sample temperature is plotted versus current is not reproduced when plotted versus Joule power. In panels a and e we plot the sample resistance as a function of current. In panels b and f we plot the sample temperature as a function of voltage, which does not collapse as shown for sample 2 in the main text. In panels c and g we plot the output noise power spectral density P/k_B as a function of current, which also does not fully collapse as sample temperature does. In panels d and h we plot the sample temperature as a function of Joule power given by $P_{\text{Joule}} = IV$, where the curves again do not collapse to the same extent as when plotted versus current.

We also investigate the criticality of the SIT by comparing the zero-bias resistance of the sample with the high-bias resistance. Shown in Fig. S8, we plot the ratio of the zero-bias and high-bias resistances as a function of gate voltage for each sample. We look for the critical point of the SIT, identified by resistance which is temperature-independent, meaning that zero-bias and high-bias resistances are equal. When plotted as the ratio of resistance at zero-bias to the resistance at high-bias, the SIT would occur around 1, marked by the dark blue line in each panel with ‘SIT’ written vertically. The superconducting (S, lilac), anomalous metallic (AM, yellow), and insulating (I, green) regions are indicated in Fig. S8. The transition from anomalous metallic to insulating behavior marks also the SIT, as determined in Fig. 2a at the separatrix whose zero-bias resistance is about 60 k Ω . This is also the point where the ratio of zero-bias to high-bias resistance is close to or equal to one.

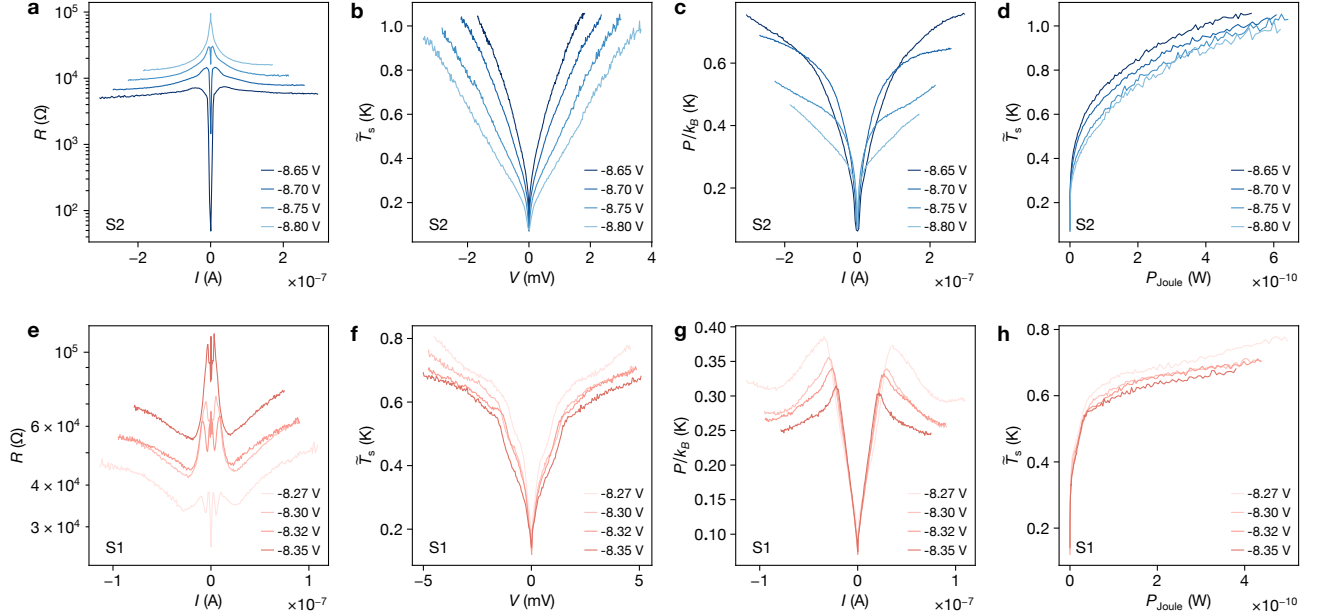


FIG. S7. **Finite bias noise data.** **a** Sample 1 resistance plotted as a function of current. **b-d** Sample temperature plotted as a function of voltage, output noise spectral density, or power does not fully collapse. **d** Sample 2 resistance plotted as a function of current. **e-f** Sample temperature plotted as a function of voltage, output noise spectral density, or power does not fully collapse.

Wide frequency sweep

To investigate the frequency dependence of the reflection parameter we measured in a wider band around the frequency of our noise signal (1.42 GHz). We show in Fig. S9a the dependence of $|S_{11}|$ on gate voltage and frequency. Overlaid in red is the DC resistance measured simultaneously, showing that the resistive state appears just after the thin dip in $|S_{11}|$ and continues throughout the wider dip region before becoming immeasurably large at the most negative gate voltages. There is a resonance in $|S_{11}|$ around -7.25 V, deep in the superconducting regime, which does

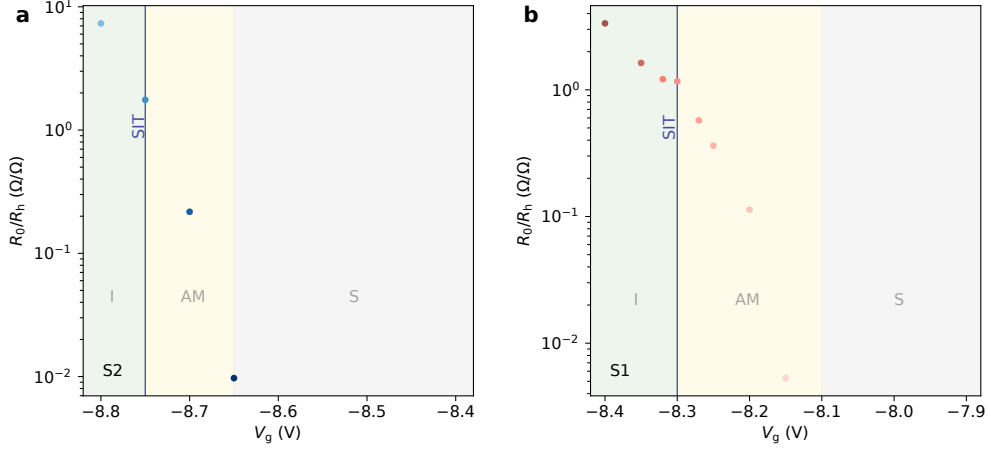


FIG. S8. **Ratio between zero and high bias resistances.** **a** The ratio of the resistance at zero bias, R_0 , to the resistance at high bias, R_h , plotted as a function of gate voltage for sample 2. **b** The same ratio as a function of gate voltage for sample 1. In both panels regions of superconducting, S, anomalous metallic, AM, and insulating, I, behavior are indicated. The regions are designated based on the zero-bias behavior of the traces.

not change with frequency. In contrast, the thin, pronounced dip which crosses 1.42 GHz at about -7.75 V, has a strong frequency dependence. The larger dip spanning -7.8 to -8.25 V does not have a strong frequency dependence. Similarly, in Fig. S9b we plot the same $|S_{11}|$ as a function of gate voltage and frequency, but with the simultaneously measured P/k_B overlaid in red. The quantity P/k_B was measured in the usual 10 MHz band around 1.42 GHz. The features in $|S_{11}|$ are reproduced in by the measured noise, P/k_B .

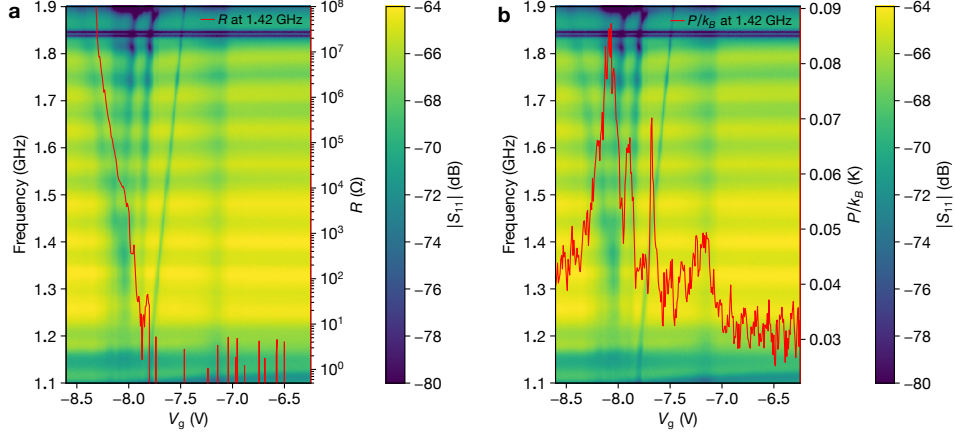


FIG. S9. **Wide frequency S_{11} sweep.** **a** In a wide frequency band $|S_{11}|$ (color bar) is plotted as a function of frequency and gate voltage. Sample resistance is plotted in red on the right axis as a function of gate voltage. **b** The same $|S_{11}|$ is plotted as a function of gate voltage and frequency with P/k_B plotted in red on the right axis as a function of gate voltage.

Magnetic field

We apply a perpendicular magnetic field of 200 mT to drive the sample to the normal state in order to study properties of the normal state. All measurements in Fig. S10 are performed at zero gate voltage. As shown in Fig. S10a on the left axis, the normal state resistance is bias independent and about 94Ω . On the right axis we observe nearly bias-independent (less than half a dB) $|S_{11}|$, about 8.5 dB below our calibrated unity reflection of -64.5 dB. In Fig. S10b, the sample temperature is plotted as a function of current, where a pronounced sub-linear behavior is observed. Lastly, we examine scaling behavior in the normal state. For high bias we expect the electron-phonon relaxation to be the dominant mechanism, thus we expect $P_{\text{Joule}} = \Sigma VT^5$, where Σ is the coupling constant,

V is the volume, and T is the temperature [40]. Fitting to the curve of sample temperature versus power $P_{\text{Joule}} = IV$ in Fig. S10c, we find a scaling relationship above 1 nW. The scaling exponent of 0.22 is in good agreement with the predicted value of $1/5$. Having validated the electron-phonon nature of the energy relaxation we can then fit to the fixed exponent P_{Joule} vs T_s^5 curve to find the coupling constant, Σ . Assuming the relevant volume of the sample is $V = 7.4 \times 10^{-17} \text{ m}^3$ (given by the sample width of $46 \mu\text{m}$, length of $115 \mu\text{m}$, and depth of 14 nm), we divide the resulting slope by the volume to obtain a coupling constant $\Sigma = 3.4 \times 10^9 \text{ Wm}^{-3}\text{K}^{-5}$.

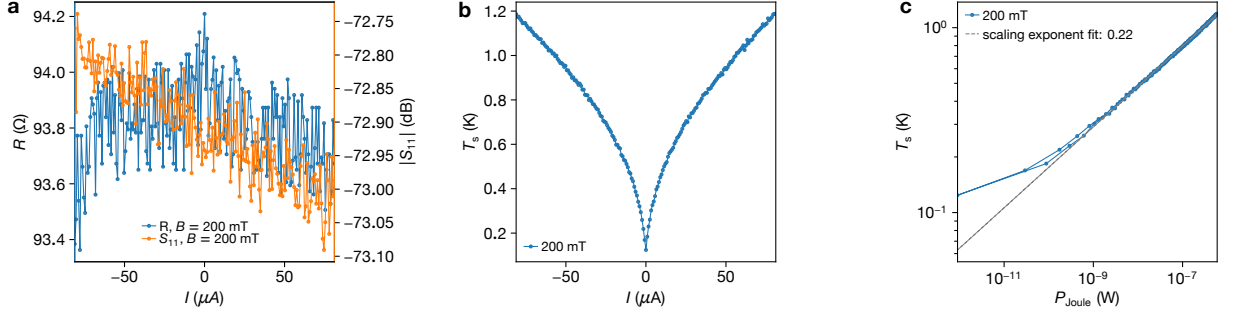


FIG. S10. **Magnetic field sweep.** **a** Resistance as a function of current plotted on the left axis in blue. $|S_{11}|$ as a function of current plotted on the right axis in orange. Resistance and $|S_{11}|$ are essentially unchanged over this bias range. $|S_{11}|$ is low, about 8.5 dB below the calibrated unity reflection. **b** Sample temperature plotted as a function of current. The slope is higher at low bias, and lower at high bias. **c** Sample temperature plotted as a function of power, $P_{\text{Joule}} = IV$. At higher powers there is a scaling relationship with exponent approximately $1/5$.

Additional sample

A previous sample was loaded to the dilution refrigerator in a different measurement configuration without the cryogenic switch to perform calibration in-situ. The measurement setup had less filtering and higher noise level than the setup used in this work and presented in Fig. S1. This sample had a slightly different four-probe measurement geometry but was fabricated of a similar Al/InAs wafer and had the same number of junctions and overall orientation as sample 1 in this work. We present data in Fig. S11 to demonstrate another anomalous metal device with corresponding excess noise spike at the onset of resistance saturation. In this sample, in the less well-filtered measurement chain, we observe a massive spike in excess noise, of nearly 500 mK, which roughly corresponds to the cryostat temperature at the onset of resistance saturation. In this case the noise P'/k_B was calibrated by taking a temperature sweep and performing a linear fit to extract the gain (in W/K), and then dividing the noise power measured by the gain to get the value in K . The added noise temperature due to the amplifier is not calibrated out. No responsivity curve or detailed hot-cold calibration with 50Ω caps was performed.

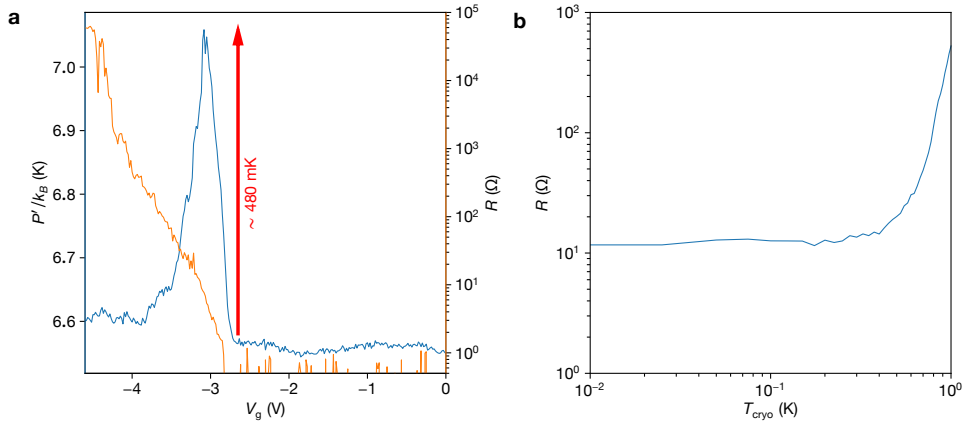


FIG. S11. Noise peak in an additional sample.